# Metal-to-Ligand Charge Transfer Photochemistry: Homolysis of the Mn−Cl Bond in the *mer*-Mn(Cl)(CO)$_3$(α-diimine) Complex and Its Absence in the *fac*-Isomer

**Angela Rosa,*,† Giampaolo Ricciardi,† Evert Jan Baerends,*,‡ and Derk J. Stufkens§**

Dipartimento di Chimica, Università della Basilicata, Via N. Sauro, 85, 85100 Potenza, Italy, Afdeling Theoretische Chemie, Vrije Universiteit, De Boelelaan 1083, 1081 HV Amsterdam, The Netherlands, and Anorganisch Chemisch Laboratorium, Nieuwe Achtergracht 166, Universiteit van Amsterdam, 1018 WV Amsterdam, The Netherlands

*Received July 1, 1998*

Homolytic breaking of the axial metal−Cl bond is not observed upon irradiation at 488 nm of either *fac*-Mn(Cl)(CO)$_3$(α-diimine) or the parent Mn(Cl)(CO)$_5$. Surprisingly, it does occur for the equatorial Mn−Cl bond in several *mer*-Mn(Cl)(CO)$_3$(α-diimine). Using DFT calculations it is shown that this photochemical homolysis can only be understood if strong relaxation of the metal fragment occurs concurrent with the equatorial Cl departure, releasing sufficient energy to make the photodissociation energetically possible. The unrelaxed metal fragment with an equatorial vacancy would be very unstable (by 116 kJ/mol) with respect to the relaxed fragment with an axial vacancy. The migration of an axial CO to the equatorial site invoked in the proposed photodissociation mechanism does not occur on the potential energy surface of the photoactive excited state, which is bound in the Mn−Cl dissociation coordinate. It is proposed to occur in a continuum state (above the asymptotic energy) of the ground-state potential energy surface that is in resonance with the photoactive excited state. The possible importance of this mechanism for TM complex photochemistry, where rearrangement of ligands may often occur upon photodissociation, is stressed.

## Introduction

The transition metal complexes containing an α-diimine ligand such as bpy (2,2′-bipyridine), phen (1,10-phenanthroline), or R-DAB (substituted 1,4-diaza-1,3-butadiene) have very low-lying metal-to-ligand charge transfer (MLCT) states which belong to transitions from the metal to the lowest $\pi^*$ orbital of the α-diimine ligand. Although MLCT states are usually unreactive and have long lifetimes, the photoreactivity (homolysis of M−X or M−R bonds or photodissociation of a carbonyl ligand) of these low-lying MLCT states is now experimentally well-documented, e.g. for M(CO)$_4$(α-diimine) (M = Cr, Mo, W),[1] M′(CO)$_3$(α-diimine) (M′ = Fe, Ru),[2] Ni(CO)$_2$(α-diimine),[3] *fac*-Mn(X)(CO)$_3$(α-diimine) (X = halide),[4] M(R)(CO)$_3$(α-diimine) (M = Mn, Re; R = methyl, ethyl, benzyl),[5] Ru(X)(R)(CO)$_2$(α-diimine) (X = halide; R = isopropyl)[6] and the roles of LF versus CT excited states have been carefully considered.[7]

Especially the complexes *fac*-Mn(X)(CO)$_3$(α-diimine) show a remarkable photochemical behavior. Upon irradiation into the lowest-energy MLCT band these complexes undergo release of a carbonyl ligand. According to the reaction sequence of Scheme 1, the CO-loss photoproduct reacts back thermally and photochemically with the carbonyl ligand to give the *mer*-isomer. The photochemical reaction mechanism, which in this case involves photodissociation of an equatorial CO with a concurrent movement of the axial X to the equatorial position, has been elucidated in ref 10. The *mer*-isomer, however, exhibits a very different photochemistry[4] for α-diimine = bpy and $^{i}$Pr-PyCa (pyridine-2-carbaldehyde *N*-isopropylimine): it photodecomposes into the radicals X$^{\bullet}$ and [Mn(CO)$_3$(α-diimine)]$^{\bullet}$. The [Mn(CO)$_3$(α-diimine)]$^{\bullet}$ radicals dimerize to give Mn$_2$(CO)$_6$(α-diimine)$_2$.

The intriguing difference in primary photoprocess of the *fac*- and *mer*-isomers will be the subject of the present paper. Whereas the *fac*-isomer does not undergo Mn−X homolysis but loses CO, the *mer*-complexes do exhibit a Mn−X homolysis reaction. This is the first example of such a homolysis reaction for this class of metal carbonyl halide complexes. It has not been observed either in the parent MnX(CO)$_5$ complexes. Several studies of metal pentacarbonyl halides show that CO

* Corresponding authors.
† Università della Basilicata.
‡ Vrije Universiteit.
§ Universiteit van Amsterdam.

(1) (a) Balk, R. W.; Snoeck, Th. L.; Stufkens, D. J. Oskam, A. *Inorg. Chem.* **1980**, *19*, 9, 3015. (b) van Dijk, H. K.; Servaas, P. C.; Stufkens, D. J.; Oskam, A. *Inorg. Chim. Acta* **1985**, *104*, 179. (c) Wieland, S.; Bal Reddy, K.; van Eldik, R. *Organometallics* **1990**, *9*, 1802. (d) Víchová,J.; Hartl, F.; Vlceck, A., Jr. *J. Am. Chem. Soc.* **1992**, *114*, 10903. (e) Lindsay, E.; Vlcek, A., Jr.; Langford, C. H. *Inorg. Chem.* **1993**, *32*, 2269. (f) Vlcek, A., Jr.; Víchová, J.; Hartl, F. *Coord. Chem. Rev.* **1994**, *132*, 167.

(2) (a) Kokkes, M. W.; Stufkens, D. J.; Oskam, A. *J. Chem. Soc., Dalton Trans.* **1984**, 1005. (b) van Dijk, H. K.; Stufkens, D. J.; Oskam, A. *J. Am. Chem. Soc.* **1989**, *111*, 541. (c) van Dijk, H. K.; Kok, J. J.; Stufkens, D. J.; Oskam, A. *J. Organomet. Chem.* **1989**, *362*, 163.

(3) Servaas, P. C.; Stufkens, D. J.; Oskam, A. *Inorg. Chem.* **1989**, *28*, 1780.

(4) (a) Stor, G. J.; Morrison, S. L.; Stufkens, D. J. Oskam, A. *Oganometallics* **1994**, *13*, 2641. (b) Kleverlaan, C. J.; Hartl, F.; Stufkens, D. J. *Photochem. Photobiol.* A **1997**, *103*, 231.

(5) (a) Lucia, L. A.; Burton, R. D.; Schanze, K. S. *Inorg. Chim. Acta* **1993**, *208*, 103. (b) Rossenaar, B. D.; Kleverlaan, C. J.; van de Ven, M. C. E.; Stufkens, D. J.; Vlcek, A., Jr. *Chem. Eur. J.* **1996**, *2*, 228. (c) Rossenaar, B. D.; Stufkens, D. J.; Oskam, A. *Inorg. Chim. Acta* **1996**, *247*, 215.

(6) Nieuwenhuis, H. A.; van de Ven, M. C. E.; Stufkens, D. J.; Oskam, A.; Goubitz, K. *Organometallics* **1995**, *14*, 780.

(7) Vlcek, A., Jr.; Víchová, J.; Hartl, F. *Coord. Chem. Rev.* **1994**, *132*, 167.

10.1021/ic980757f CCC: $15.00 
Published on Web 11/11/1998

**Scheme 1**

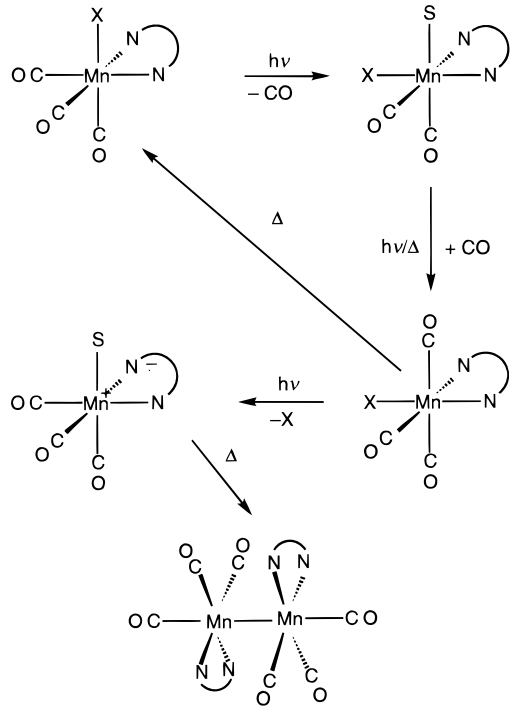

loss is the primary photoprocess.[8] We have recently studied[9] the photochemistry of $Mn(Cl)(CO)_5$ by DFT calculations and have shown that the reason for the absence of Mn−Cl homolysis is the high thermodynamic stability of the Mn−Cl bond. Mn−Cl homolysis requires indeed much more energy than CO dissociation and excitation into the lowest MLCT states does not supply enough energy to homolytically break the Mn−Cl bond.

In the $Mn(X)(CO)_3$(α-diimine) complexes, the MLCT states, now involving the low-lying virtual $\pi^*$ orbitals of α-diimine rather than the CO $\pi^*$, are lower than in $Mn(Cl)(CO)_5$. No Mn−Cl bond breaking is therefore expected.

A possible clue to the observed photodissociation of the equatorial Cl of the *mer*-isomer may be obtained from the explanation given earlier[10] for the equatorial CO dissociation in the *fac*-isomer. In the latter case, the low energy of the MLCT states in the (α-diimine) complexes also poses a problem for the photodissociation. In fact, the mechanism of CO photodissociation that we have found to be operative in $Mn(CO)_5L$ (L = Cl,[9] $Mn(CO)_5$[11]) systems and in $Cr(CO)_6$[12] does not apply in this case. CO dissociation in the $M(CO)_5L$ systems was shown to occur by the system crossing over from nondissociative MLCT states to dissociative LF states. The latter are high-lying at the equilibrium geometry but descend rapidly upon M−CO bond lengthening, so they cross with the nondissociative lower MLCT states very soon, i.e., after only little elongation of the Mn−CO bond lengths. In the *fac*-$Mn(X)(CO)_3$(α-diimine), however, the MLCT states invloving α-diimine $\pi^*$ are so low that the crossing with the downcoming LF state occurs only at much lengthened Mn−CO distance, if at all. These MLCT states therefore exhibit a distinct bonding minimum around $R_e$, i.e., are not dissociative. The loss of an equatorial CO ligand in the *fac*-isomer could, however, be explained by an altogether different mechanism which involves a strong, energy lowering, rearrangement of the complex. This rearrangement consists of a shift of the axial chloride to the equatorial open site during the $Mn-CO_{eq}$ dissociation. This movement also naturally explains the photochemical *fac* → *mer* photoisomerization.

One may wonder if a similar mechanism, involving strong rearrangement of the complex during the equatorial ligand dissociation, might be operative in the case of homolytic splitting of the bond of Mn to an equatorial Cl in the *mer*-$Mn(X)(CO)_3$(α-diimine). In this paper the different behavior of the *fac*- and *mer*-$Mn(X)(CO)_3$(α-diimine) isomers with respect to the Mn−X homolysis photoreaction will be highlighted and the hypothesis of a dissociation route for this reaction involving a structural rearrangement of the system will be explored. To this end we have calculated, using a density functional approach, the ground- and excited-state potential energy curves (PECs) for the homolysis of the Mn−Cl bond of the model complexes *fac*-Mn(Cl)(H-DAB) and *mer*-Mn(Cl)(H-DAB) (H-DAB = 1,4-diaza-1,3-butadiene) (reactions 1 and 2):

$$fac\text{-}Mn(Cl)(CO)_3(\text{H-DAB}) \xrightarrow{h\nu} [Mn(CO)_3(\text{H-DAB})]^{\bullet} + Cl^{\bullet} \quad (1)$$

$$mer\text{-}Mn(Cl)(CO)_3(\text{H-DAB}) \xrightarrow{h\nu} [Mn(CO)_3(\text{H-DAB})]^{\bullet} + Cl^{\bullet} \quad (2)$$

Similarities to and differences from an aromatic α-diimine ligand like bipyridine, which would be too computationally expensive in view of the many calculations required for the PECs, will be discussed.

## 2. Method and Computational Details

The density functional calculations reported in this paper have been carried out with the Amsterdam Density Functional (ADF) program system.[13] The computational scheme is characterized by a density fitting procedure to obtain the Coulomb potential[13d] and by elaborate 3D numerical integration techniques[13b,c] for the evaluation of the Hamiltonian matrix elements, including those of the exchange-correlation potential. The density functionals included Becke's[14] gradient correction to the local exchange expression and Perdew's[15] gradient correction to the LDA expression (VWN[16] parametrization of electron gas data) for the correlation energy. The geometry optimizations have been performed at this (NL-SCF) level of theory using gradient

(8) (a) McHugh, T. M.; Rest, A. J.; Taylor, D. J. *J. Chem. Soc., Dalton Trans.* **1980**, 1803. (b) Wrighton, M. S.; Morse, D. L.; Gray, H. B.; Otteson, D. K. *J. Am. Chem. Soc.* **1976**, *98*, 1111.
(9) Wilms, M. P.; Baerends, E. J.; Rosa, A.; Stufkens, D. J. *Inorg. Chem.* **1997**, *36*, 1541.
(10) Rosa, A.; Ricciardi, G.; Baerends, E. J.; Stufkens, D. J. *J. Phys. Chem.* **1996**, *100*, 0, 15346.
(11) (a) Rosa, A.; Ricciardi, G.; Baerends, E. J.; Stufkens, D. J. *Inorg. Chem.* **1995**, *34*, 3425. (b) Rosa, A.; Ricciardi, G.; Baerends, E. J.; Stufkens, D. J. *Inorg. Chem.* **1996**, *35*, 2886.
(12) Pollak, C.; Rosa, A.; Baerends, E. J. *J. Am. Chem. Soc.* **1997**, *119*, 9, 7324.
(13) (a) Baerends, E. J.; Ellis, D. E.; Ros, P. *Chem. Phys.* **1973**, *2*, 42. (b) Boerrigter, P. M.; te Velde, G.; Baerends, E. J. *Int. J. Quantum Chem.* **1988**, *33*, 87. (c) te Velde, G.; Baerends, E. J. *J. Comput. Phys.* **1992**, *99*, 84. (d) Fonseca Guerra, C.; Visser, O.; Snijders, J. G.; te Velde, G.; Baerends, E. J. In *Methods and Techniques in Computational Chemistry*; Clementi, E., Corongiu, C., Eds.; STEF: Cagliari, Italy, 1995; Chapter 8, p 305. (e) Krijn, J.; Baerends, E. J. *Fit Function in the HFS-Method*; internal report (in Dutch): Vrije Universiteit: Amsterdam, The Netherlands, 1984.
(14) (a) Becke, A. D. *J. Chem. Phys.* **1986**, *84*, 4524. (b) Becke, A. D. *Phys. Rev.* ***1988***, *A38*, 3098.
(15) Perdew, J. P. *Phys. Rev.* ***1986***, *B33*, 8822 (Erratum: *Phys. Rev.* **1986**, *B34*, 7406).
(16) Vosko, S. H.; Wilk, L.; Nusair, M. *J. Can. J. Phys.* **1980**, *58*, 1200.

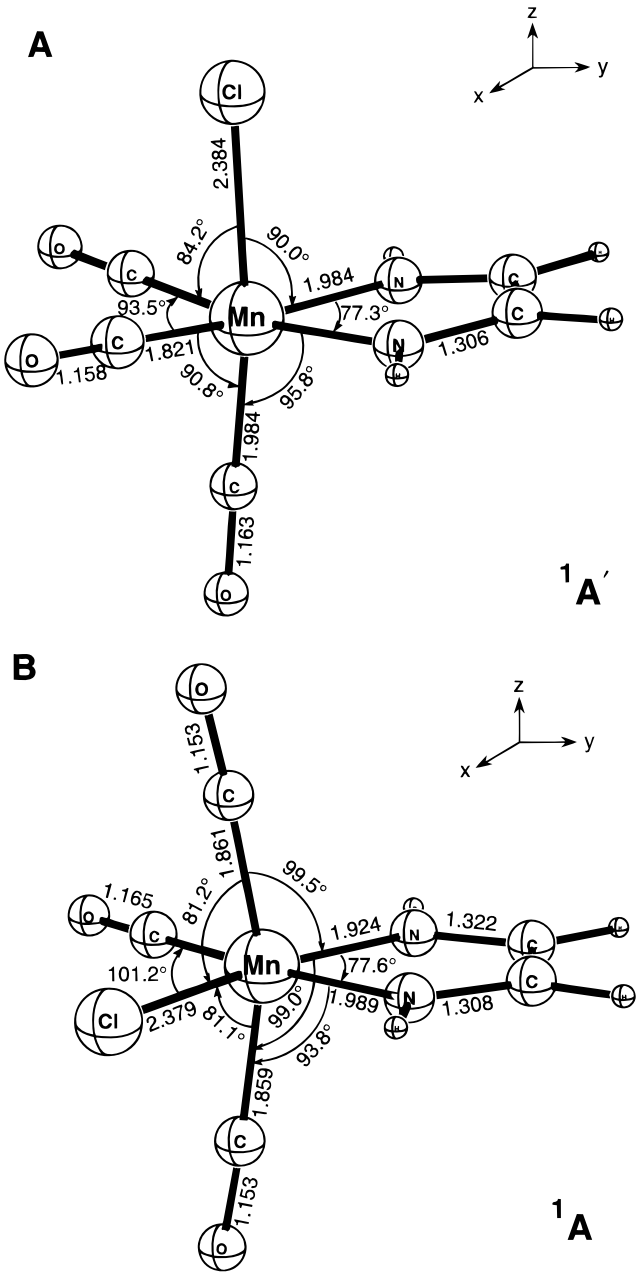


**Figure 1.** Optimized structures of (A) *fac*-Mn(Cl)$(CO)_3$(H-DAB) in $C_s$ and (B) *mer*-Mn(Cl)$(CO)_3$(H-DAB) in $C_1$ symmetry (bond distances in Å).

techniques.[17] An uncontracted triple-ζ STO basis set has been used for the C, N, O, Cl, and H atoms, with one 3d polarization function added on C, N, O, and Cl and one 3d and one 2p set added on H. For the manganese atom a triple-ζ 3d, 4s with three 4p functions was used. The cores (C, N, O, 1s; Mn, Cl, 1s2p) have been kept frozen.

We use a ΔSCF type method[18] for the calculation of excited states. This method has been used with good results for atomic[19−21] and molecular systems,[18,22−24] as well as to the potential energy surface for the photodissociation of $H_2O$ in its first excited state.[25] The results of the ΔSCF method are comparable to those of the theoretically better founded time-dependent DFT method[26,27] using the adiabatic local-density approximation, which has recently been applied successfully to a number of simple atoms[28] and molecules.[29]

In its simplest form the method of ref 18 incorporates the relaxation effects in the excited states by an SCF calculation on a single-determinant state representing one of the multiplet states.

This method is however only formally justified for the lowest states of each symmetry, although it yields results which are in keeping with experiment for a number of higher excited states as well. We are therefore aware that the energies that are not the lowest of a given symmetry are reliable only at a semi-quantitative level. As for the present case we will keep in mind the possibly larger errors for those excited-state energies and we will avoid overinterpreting them. The calculations were carried out for the *fac*- and *mer*-Mn(Cl)$(CO)_3$(H-DAB) model complexes in their optimized geometries shown in Figure 1. The optimized structure of the *fac*-Mn(Cl)$(CO)_3$(H-DAB) that we have recently calculated[10] has not been retained in this work, for sake of homogeneity with the present calculations. The previous geometry optimization was performed at the LDA level of theory using a basis set smaller than the present one.

It has been assumed that the $C_s$ symmetry is retained along the reaction path corresponding to the homolysis of the Mn−Cl bond in the *fac*-isomer (Scheme 2).

Support for this assumption comes from the fact that full geometry optimization of the **1a** (Chart 1) structure of the Cl• loss product, [Mn$(CO)_3$(H-DAB)]•, gives a structure of $C_s$ symmetry as the most stable one (vide infra). All geometrical

**Scheme 2**

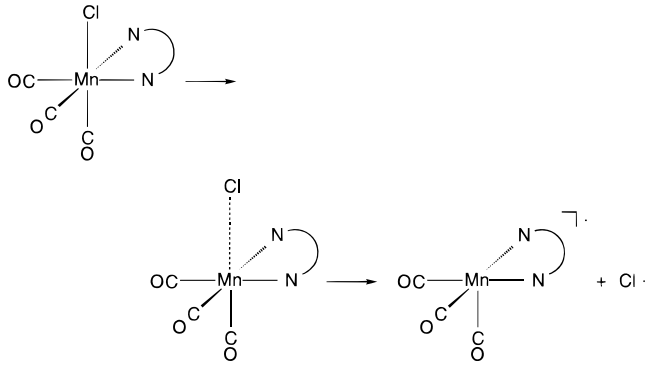


**Chart 1**

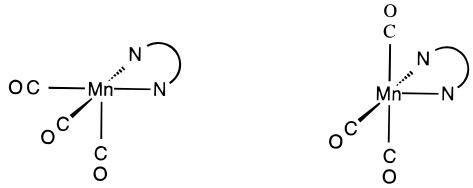


**1a** **1b**

(17) Versluis, L.; Ziegler, T. *J. Chem. Phys.* **1988**, *88*, 322.
(18) Ziegler, T.; Rauk, A.; Baerends, E. J. *Theor. Chim. Acta* **1977**, *43*, 261.
(19) von Barth, U. *Phys. Rev.* **1979**, *A20*, 1693.
(20) Wood, J. H. *J. Phys. B: Atom. Mol. Phys.* **1980**, *13*, 1.
(21) Lannoo, M.; Baraff, G. A.; Schlüter, M. *Phys. Rev.* **1981**, *B24*, 943.
(22) Ziegler, T.; Rauk, A. *Theor. Chim. Acta* **1977**, *46*, 1.
(23) Rosa, A.; Baerends, E. J. *Inorg. Chem.* **1994**, *33*, 584.
(24) Daul, C.; Baerends, E. J.; Vernooijs, P. *Inorg. Chem.* **1994**, *33*, 3543.
(25) Doublet, M. L.; Kroes, G. J.; Baerends, E. J.; Rosa, A. *J. Chem. Phys.* **1995**, *103*, 2538.
(26) Runge, E.; Gross, E. K. U. *Phys. Rev. Lett.* **1984**, *52*, 997.
(27) Gross, E. U. K.; Kohn, W. *Adv. Quantum Chem.* **1990**, *21*, 255.
(28) Petersilka, M.; Gossmann U. J.; Gross, E. K. U. *Phys. Rev. Lett.* **1996**, *76*, 1212.
(29) Jamorski, C.; Casida, M.; Salahub, D. R. *J. Chem. Phys.* **1996**, *104*, 5134.

**Scheme 3**

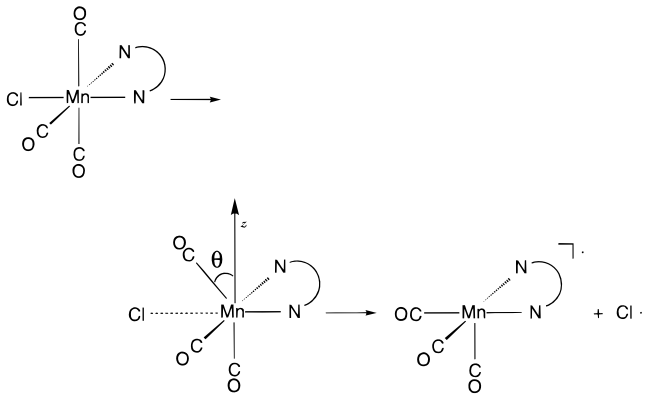

parameters, except for the dissociating bond, were kept constant along the reaction pathway. This choice is justified by the fact that the unrelaxed **1a** structure of the five-coordinated fragment does not differ significantly from the optimized one.

For the dissociation of the equatorial Cl• in the *mer*-Mn(Cl)-$(CO)_3$(H-DAB), the angle $\theta$ that the axis of one of the Mn−$CO_{ax}$ bonds makes with the vertical *z* axis has been optimized along the Mn−Cl coordinate (Scheme 3). This choice was inspired by the fact that optimization starting at the **1b** structure of the five-coordinated fragment corresponding to the removal of the equatorial Cl• radical from *mer*-Mn(Cl)$(CO)_3$(H-DAB) affords the same $C_s$ structure as that obtained by optimization of the **1a** fragment, which implies that one axial CO has shifted to the vacant equatorial site. Furthermore, the dissociation process is believed to be slow (vide infra), which would allow the system to relax during Cl• departure.

### 3. Ground State Electronic Structure

The first step to understand the different photochemical behavior of the *fac*- and *mer*-isomers with respect to the homolysis of the Mn−Cl bond is to compare their electronic structures. Table 1a exhibits the energies and compositions of the orbitals of the *fac*-isomer, to which we shall need to refer several times in the following. We refer to our recent studies[10] for a detailed discussion of the electronic structure of *fac*-Mn-(Cl)$(CO)_3$(H-DAB).

The characters and the orbital energies of the highest occupied and lowest unoccupied MOs of the *mer*-Mn(Cl)$(CO)_3$(H-DAB) are presented in Table 1b, in terms of Mn, Cl, $CO_{ax}$, $CO_{eq}$, and H-DAB fragment orbitals, which can be compared to the same information for *fac*-Mn(Cl)$(CO)_3$(H-DAB) in Table 1a. The level pattern is very similar in the two isomers, corresponding to a $3d^6$ Mn in a pseudooctahedral environment, although the structural change has some influence on the energy and composition of the one-electron levels.

In the occupied spectrum of the *mer*-Mn(Cl)$(CO)_3$(H-DAB) we have, above the Cl-$p_\sigma$ (32a), the Cl-$p_\pi$ orbitals and the metal−carbonyl $\pi$-bonding $t_{2g}$-like 3d orbitals. The 36a and 37a are the $\pi$ antibonding and the 33a and 34a the $\pi$ bonding combinations of $3d_\pi$ and Cl-$p_\pi$ orbitals, while the 35a ($d_{yz}$) does not mix with Cl AOs but remains a pure $3d_\pi$-CO $2\pi^*$, H-DAB $\pi^*$ bonding orbital (cf. the choice of axes in Figure 1). It is noteworthy that the relative Mn-3d and Cl-3p character of the Mn−Cl bonding/antibonding pairs is reversed compared to the *fac*-isomer. In the *mer*-Mn(Cl)$(CO)_3$(H-DAB) the Mn−Cl $\pi$ bonding orbitals have predominantly Cl-$3p_\pi$ character, whereas the antibonding counterparts are mainly Mn-$d_\pi$.

The virtual orbitals are particularly relevant in view of the photochemistry. In both isomers we find that the LUMO (the 24a′ in the *fac*- and 38a in the *mer*-isomer) has mainly H-DAB $\pi^*$ character, with the H-DAB $\pi^*$ participating for more than 70% in this orbital. The important implication is that the lowest excited states will have in both isomers CT (MLCT or XLCT) character.

As inferred from Tables 1a and 1b, in the *mer*-Mn(Cl)$(CO)_3$-(H-DAB) a noticeably smaller gap than in the *fac*-isomer (0.9 vs 2 eV) separates the LUMO from the virtual orbitals of (mostly) CO $2\pi^*$ and Mn $d_{xy}$, $d_{z^2}$ ("$e_g$") character. We have observed that in the *fac*-Mn(Cl)$(CO)_3$(H-DAB) the $d_{xy}$, $d_{z^2}$ AO's are divided over two sets of virtual orbitals, the lower 15a″ and 25a′ having little antibonding with the equatorial and axial CO $5\sigma$ lone pairs, respectively, and the higher 18a″ and 28a′ having strong antibonding with these CO lone pairs. Similar orbital interactions also occur in the *mer*-isomer, but due to the lower symmetry the effect is less distinct. We find in fact the $d_{z^2}$ and $d_{xy}$ orbitals to be spread out over a large set of virtual levels. Among these, only the high lying 43a has both strong Mn−$CO_{eq}$ and Mn−$CO_{ax}$ $\sigma$ antibonding character. It is somewhat analogous to the 18a″ and 28a′ of the *fac*-(Cl)Mn-$(CO)_3$(H-DAB) and we denote its $\sigma$ antibonding character with CO $5\sigma$ again with a prime: $e_g'(\sigma^{*\prime})$. The present study focuses on the photodissociation of the Mn−Cl bond, for which the Mn−Cl $\sigma$ antibonding orbital (denoted $\sigma^*$, without a prime) is of primary interest. In the *mer*-isomer this is the 39a, containing a considerable amount of $d_{xy}$ as well as $d_{z^2}$ character, strongly antibonding with the Cl-$p_\sigma$. It has no Mn−$CO_{eq}$ and very weak Mn−$CO_{ax}$ $\sigma$ antibonding character and is, in line with the weaker $\sigma$ donor capability of Cl compared to CO, at considerably lower energy than the $\sigma^{*\prime}$. This orbital is analogous to the 25a′ of the *fac*-isomer, see Figure 2b of ref 10. The 39a has, together with the 40a, also antibonding with the N lone pairs of the α-diimine.

The remaining orbitals in the virtual spectrum, which are straddled by the $e_g(\sigma^*)$ and $e_g'(\sigma^{*\prime})$, consist of predominantly CO $2\pi^*$ orbitals.

### 4. Excited States and Electronic Spectra

The absorption spectra of *fac*- and *mer*-Mn(X)$(CO)_3$(α-diimine) (X = halide) complexes are characterized by two rather strong bands in the UV/vis region.[4,30,31] Their position strongly depends on the α-diimine ligand and X. A shift to lower energy occurs when an aromatic α-diimine ligand such as bpy is replaced by a nonaromatic one such as R-DAB (R = $^i$Pr, $^t$Bu, pTol, etc.) having the first available $\pi^*$ orbital at lower energy. These bands have been assigned to charge-transfer transitions to the $\pi^*$ of the α-diimine ligand on the basis of the dependence of the position of the bands on the substituents of the α-diimine ligand, and on the basis of the strong solvatochromism and of the resonance enhancement, upon excitation in these bands, of Raman intensity for the symmetrical stretching modes of the α-diimine ligand.

The UV/vis spectra of the two isomers of Mn(Cl)$(CO)_3$($^i$Pr-DAB), taken as prototype of Mn(Cl)$(CO)_3$(α-diimine) complexes containing an aliphatic α-diimine ligand, are displayed in Figure 2. The spectrum of the *mer*-Mn(Cl)$(CO)_3$($^i$Pr-DAB) in THF shows two absorption maxima at 600 nm (2.07 eV) and 452 nm (2.74 eV), respectively. The lowest energy band is very broad and ∼2 times less intense than the second band. In the *fac*-Mn(Cl)$(CO)_3$($^i$Pr-DAB) the two UV/vis bands are

(30) Staal, L. H.; Oskam, A.; Vrieze, K. *J. Organomet. Chem.* **1979**, *170*, 235.
(31) Stor, G. J.; Stufkens, D. J.; Vernooijs, P.; Baerends, E. J.; Fraanje, J.; Goubitz, K. *Inorg. Chem.* **1995**, *34*, 1588.

**Table 1.** One-Electron Energies and Percentage Composition (Based on Mulliken Population Analysis per MO) of the Lowest Unoccupied and Highest Occupied Orbitals in Terms of Mn, $CO_{eq}$, $CO_{ax}$, Cl, and H-DAB Fragments; Orbital Characters "$e_g$" and "$t_{2g}$" Refer to the Pseudo-Octahedral Symmetry

| MO | $\epsilon$ (eV) | orbital character | Mn | $CO_{eq}$ | $CO_{ax}$ | Cl | H-DAB |
|---|---|---|---|---|---|---|---|
| | | | (a) For *fac*-Mn(Cl)$(CO)_3$(H-DAB) | | | | |
| unoccupied orbitals | | | | | | | |
| 28a′ | −1.60 | $e_g'$ ($\sigma$*′) | 16($d_{z^2}$) | 5(5$\sigma$); 36(2$\pi^*_\perp$) | 9(5$\sigma$); 34(2$\pi$*) | − | − |
| 18a″ | −1.67 | $e_g'$ | 31($d_{xy}$) | 19(5$\sigma$); 30(2$\pi^*_{\|\|}$) | 11(2$\pi$*) | − | 9(6a″) |
| 17a″ | −1.79 | | − | 47(2$\pi^*_\perp$); 18(2$\pi^*_{\|\|}$) | 18(2$\pi$*) | − | 17(6a″) |
| 16a″ | −2.09 | | 21($d_{xz}$) | 29(2$\pi^*_\perp$); 20(2$\pi^*_{\|\|}$) | 30(2$\pi$*) | − | − |
| 27a′ | −2.11 | | 17($d_{x^2-y^2}$) | 51(2$\pi^*_{\|\|}$); 18(2$\pi^*_\perp$) | 10(2$\pi$*) | − | 4(8a′) |
| 26a′ | −2.45 | | 21($d_{yz}$); 5($d_{x^2-y^2}$); | 2(5$\sigma$); 22(2$\pi^*_\perp$); 13(2$\pi^*_{\|\|}$) | 30(2$\pi$*) | 2(3$p_z$) | 5(8a′) |
| 25a′ | −2.84 | $e_g$ ($\sigma$*) | 36($d_{z^2}$); 4(4$p_z$); | 2(5$\sigma$); 16(2$\pi^*_\perp$); 4(2$\pi^*_{\|\|}$) | 6(5$\sigma$); 10(2$\pi$*) | 14(3$p_z$) | 8(6a′) |
| 15a″ | −2.97 | $e_g$ | 26($d_{xy}$); 5(4$p_x$); 5($d_{xz}$) | 4(5$\sigma$); 28(2$\pi^*_{\|\|}$) | 16(2$\pi$*) | 1(3$p_x$) | 15(5a″) |
| 24a′ | −4.97 | H-DAB $\pi$* | 9($d_{yz}$) | 6(2$\pi^*_\perp$) | − | 7(3$p_z$) | 78(7a′) |
| occupied orbitals | | | | | | | |
| 14a″ | −5.99 | Cl-$p_\pi$-$d_\pi$ | 28($d_{xz}$) | 5(2$\pi^*_\perp$) | 6(2$\pi$*) | 61(3$p_x$) | − |
| 23a′ | −6.05 | Cl-$p_\pi$-$d_\pi$ | 16($d_{yz}$); 3($d_{x^2-y^2}$) | − | 5(2$\pi$*) | 70(3$p_y$) | 6(7a′) |
| 22a′ | −6.83 | $t_{2g}$($d_{x^2-y^2}$) | 68($d_{x^2-y^2}$); 2(4$p_y$) | 27(2$\pi^*_{\|\|}$) | − | 3(3$p_y$) | − |
| 13a″ | −7.11 | $t_{2g}$($d_\pi$+ Cl-$p_\pi$) | 41($d_{xz}$) | 13(2$\pi^*_\perp$) | 5(2$\pi$*) | 34(3$p_x$) | 7(4a″) |
| 21a′ | −7.34 | $t_{2g}$($d_\pi$+ Cl-$p_\pi$) | 45($d_{yz}$) | 6(2$\pi^*_\perp$) | 9(2$\pi$*) | 25(3$p_y$) | 15(7a′) |
| 20a′ | −7.96 | Cl-$p_\sigma$ | 8($d_{z^2}$); 7(4$p_z$); 2($d_{yz}$) | 7(2$\pi^*_\perp$) | 4(5$\sigma$) | 69(3$p_z$) | 3(7a′) |
| | | | (b) For *mer*-Mn(Cl)$(CO)_3$(H-DAB) | | | | |
| unoccupied orbitals | | | | | | | |
| 45a | −0.96 | | 11($d_{xz}$);7($d_{yz}$) | − | 77(2$\pi$*) | 5(3$p_z$) | − |
| 44a | −1.04 | | 7($d_{z^2}$);7($d_{xy}$);4($d_{x^2-y^2}$) | 5(5$\sigma$); 35(2$\pi^*_\perp$); 15(2$\pi^*_{\|\|}$) | 4(5$\sigma$); 16(2$\pi$*) | | − |
| 43a | −1.10 | $e_g'$($\sigma$*′) | 20($d_{z^2}$);13($d_{xy}$) | 9(5$\sigma$); 8(2$\pi^*_\perp$); 12(2$\pi^*_{\|\|}$) | 6(5$\sigma$); 22(2$\pi$*) | − | 7(N-lp) |
| 42a | −1.49 | | 13($d_{yz}$); 14($d_{xz}$) | 11(2$\pi^*_{\|\|}$); 22(2$\pi^*_\perp$) | 37(2$\pi$*) | − | − |
| 41a | −1.88 | | 13($d_{z^2}$); 8(4s); 12($d_{xy}$) | − | 2(5$\sigma$); 50(2$\pi$*) | − | 10(N-lp) |
| 40a | −2.14 | | 5($d_{z^2}$); 4(4$p_x$); 7($d_{xy}$) | − | 4(5$\sigma$); 72(2$\pi$*) | − | 6(N-lp) |
| 39a | −2.45 | $e_g$($\sigma$*) | 11($d_{z^2}$); 5(4$p_y$); 29($d_{xy}$) | − | 4(5$\sigma$); 25(2$\pi$*) | 14(3$p_x$); 6(3$p_y$) | 6(N-lp) |
| 38a | −3.39 | H-DAB $\pi$* | 17($d_{yz}$); 2($d_{xz}$) | − | 4(5$\sigma$); 4(2$\pi$*) | 2(3$p_z$) | 72($\pi$*) |
| occupied orbitals | | | | | | | |
| 37a | −5.14 | $t_{2g}$($d_\pi$-Cl-$p_\pi$) | 58($d_{x^2-y^2}$) | 7(2$\pi^*_{\|\|}$); 4(2$\pi^*_\perp$) | − | 17(3$p_y$); 8(3$p_x$) | − |
| 36a | −5.46 | $t_{2g}$($d_\pi$-Cl-$p_\pi$) | 38($d_{xz}$);7($d_{yz}$); 2(4$p_z$) | − | 2(2$\pi$*) | 33(3$p_z$) | 12($\pi$) |
| 35a | −6.30 | $t_{2g}$($d_{yz}$) | 47($d_{yz}$); 10($d_{xz}$) | 5(2$\pi^*_\perp$) | 13(2$\pi$*) | − | 16($\pi$*) |
| 34a | −6.54 | Cl-$p_\pi$+ $d_\pi$ | 18($d_{xz}$) | 2(5$\sigma$); 2(2$\pi^*_\perp$) | 4(5$\sigma$); 9(2$\pi$*) | 58(3$p_z$) | 5(N-lp) |
| 33a | −6.61 | Cl-$p_\pi$+ $d_\pi$ | 18($d_{x^2-y^2}$) | 2(2$\pi^*_\perp$); 2(2$\pi^*_{\|\|}$) | − | 26(3$p_x$); 47(3$p_y$) | − |
| 32a | −7.53 | Cl-$p_\sigma$ | 5($d_{z^2}$); 6($d_{xy}$); 2(4$p_x$); 3(4$p_y$) | − | − | 48(3$p_x$); 25(3$p_y$) | 5(N-lp) |

shifted to shorter wavelengths, 476 nm (2.61 eV) and 359 nm (3.45 eV), respectively, and their relative intensities are reversed with respect to the *mer*. The low-energy band of *fac*-Mn(Cl)-$(CO)_3$($^i$Pr-DAB) shows strong solvatochromism and its absorption maximum will shift to longer wavelengths in the gas phase, to which the calculations of the excitation energies apply. For the *mer*-isomer no solvent dependence could be studied since it is only produced in (weakly) coordinating solvents such as THF.

We have recently calculated the excitation energies to the lowest $^{1,3}$A′ and $^{1,3}$A″ excited states of the *fac*-Mn(Cl)$(CO)_3$-(H-DAB).[10] The lowest band was assigned to excitations from the antibonding $p_\pi$(Cl)-$d_\pi$(Mn) (14a″, 23a′) orbitals and the $d_{x2-y2}$ (22a′) orbital to the H-DAB $\pi$*. The second absorption band was assigned to two types of transitions. The first are transitions to the 24a′ H-DAB $\pi$* LUMO from the $p_\pi$-$d_\pi$ bonding $d_{xz}$(Mn)+$p_x$(Cl) and $d_{yz}$(Mn)+$p_y$(Cl) orbitals 13a″ and 21a′. The second type of transitions belonging to this band was found to be the excitations to the next higher virtual orbitals, the $e_g$ set (15a″, 25a′) which is ca. 2 ev above the H-DAB $\pi$*, out of the $p_\pi$-$d_\pi$ antibonding HOMOs 14a″, 23a′.

These assignments are largely confirmed by the more accurate (cfr. Section 2) present calculations, as can be inferred from Table 2 where the energies of the lowest $^{1,3}$A′ and $^{1,3}$A″ excited states of the *fac*-Mn(Cl)$(CO)_3$(H-DAB) are reported. Although the excitations from the "$t_{2g}$" type orbitals 14a″, 23a′, and 22a′ to the H-DAB $\pi$* can all be attributed to the first band at 2.36 eV, which is obviously calculated at too low energy, only the 23a′ → 24a′ will contribute significantly to this band, according to the calculated transition dipole moments (see Table 2). We note that this intense transition is from an orbital with considerable $d_{yz}$ character to the $\pi$*-DAB orbital. A relatively high transition dipole moment for excitation out of $d_{yz}$ to $\pi$*-DAB can be understood from a simple overlap argument for the relevant dipole matrix element. The second band contains excitations from the bonding Mn-3$d_\pi$-Cl-3$p_\pi$ orbitals 13a″ and 21a′ to the H-DAB $\pi$* as well as excitations from the antibonding Mn-3$d_\pi$-Cl-3$p_\pi$ orbitals 14a″ and 23a′ to the $e_g$ type 25a′, which is $d_{z^2}$-Cl-$p_\sigma$ antibonding (Mn−Cl$\sigma$*). We previously also assigned the transitions out of the 14a″ and 23a′ to the other $e_g$ type orbital, 15a″ ($d_{xy}$), to this second band, but the large intensity value of the 14a″ → 15a″ suggests that this transition (together with the 23a′ → 15a″ having very little intensity) contributes to the third intense maximum present in the spectrum of the *fac*-Mn(Cl)$(CO)_3$($^i$Pr-DAB) at 309 nm (4.01 eV).

The calculated energies to the lowest $^{1,3}$A excited states of *mer*-Mn(Cl)$(CO)_3$(H-DAB) and the transition dipole moments associated with the singlets are reported in Table 3. The lowest allowed excited states of the *mer*-isomer correspond to the 37a → 38a, 36a → 38a MLCT excitations which are, as in the case of the *fac*-isomer, from the $p_\pi$-$d_\pi$ antibonding orbitals to the H-DAB $\pi$*. They are calculated at 1.55 and 1.89 eV, respectively. Their corresponding triplets occur at 1.40 and 1.53 eV. Transition dipole moments reported in Table 3 show that the only transition expected to contribute to the lowest broad band centered at 600 nm (2.07 eV) is the 36a → 38a, on account probably of the $d_{yz}$ character of the 36a, which increases in the excited state.

The next singlet MLCT state, $d^1$A, is calculated at 2.55 eV (the corresponding triplet, $d^3$A, is at 2.22 eV) and corresponds to the 35a → 38a, $d_{yz(xz)}$(Mn) → $\pi$* (H-DAB), transition. It is

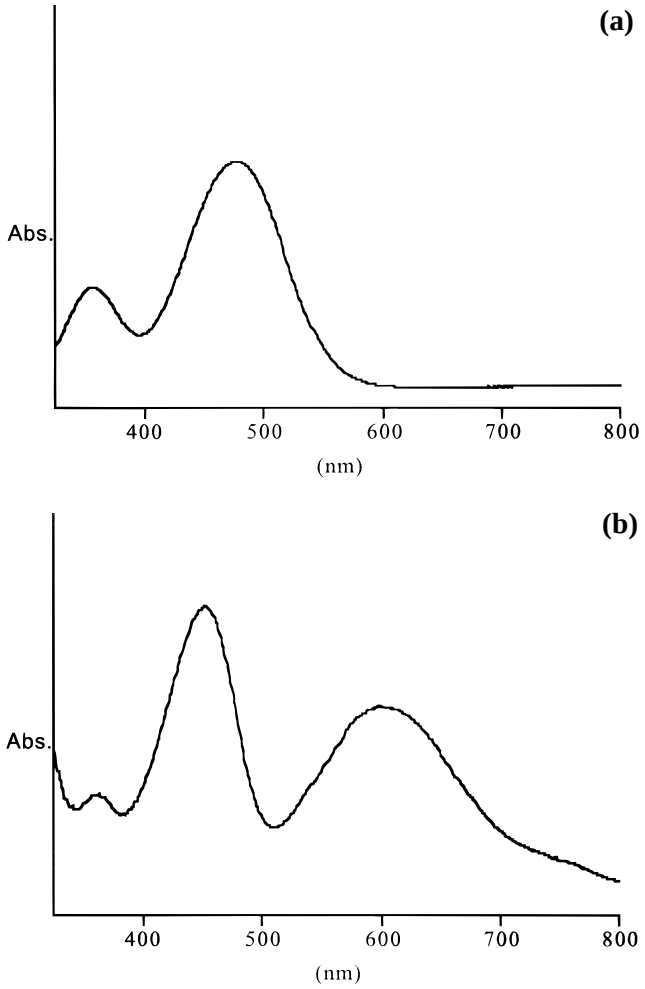


**Figure 2.** UV/vis spectra of *fac*-Mn(Cl)(CO)$_3$($^i$Pr-DAB) (a) and *mer*-Mn(Cl)(CO)$_3$($^i$Pr-DAB) (b) in THF at room temperature.

expected to contribute significantly to the intense second absorption band. We note that the associated transition dipole moment is almost 2 times larger than the one calculated for the lower-lying $c^1A$ (36a → 38a) MLCT state, in agreement with the 1:2 intensity ratio of the two lowest experimental bands. We observed for the *fac*-isomer that high intensity derives from a large $d_{yz}$ to $\pi^*$ (H-DAB) transition dipole moment. However, in the *fac*-isomer the $d_{yz}$ is pushed up by antibonding with the Cl $p_\pi$, so the $d_{yz}$-to-$\pi^*$ (H-DAB) intensity primarily contributes to the first band. In the *mer*-isomer it is the nonbonding (with respect to Cl) orbital 35a that has a large $d_{yz}$ character, although there is also some $d_{yz}$ character in the high-lying 36a, contributing to the intensity of the first band. The 35a orbital is almost 1 eV below the Mn−Cl antibonding 36a, and the excitation energy to the $\pi^*$-DAB is so much higher that this excitation belongs to the second band. The change of $d_{yz}$ from Mn−Cl $\pi$ antibonding in the *fac*-isomer to nonbonding in the *mer*-isomer accounts at least partly for the observed reversal of the intensity distribution over the first and second bands when going from the *fac*- to the *mer*-isomer.

The $e^1A$ and $f^1A$ states computed at 2.72 and 2.99 eV will also contribute to the second band. These states correspond to the 37a → 39a, 36a → 39a, d → d transitions which are from the antibonding $d_{x^2-y^2}$(Mn)-$p_{\pi x,y}$(Cl), $d_{xz,yz}$(Mn)-$p_{\pi z}$ (Cl) orbitals to the $\sigma^*$(Mn−Cl) and have low intensity. The corresponding triplets are computed at 2.15 and 2.57 eV. There is a relatively large singlet/triplet splitting due to the partial localization of the unpaired electrons on the metal center.

There is next a set of transitions, out of the $p_\pi$-$d_\pi$ antibonding HOMOs to the mostly CO $2\pi^*$ levels 40a and 41a, which can be assigned to the third band. Unlike in the *fac*-isomer, in the *mer*-Mn(Cl)(CO)$_3$(H-DAB) the transitions from the bonding $d_\pi$-(Mn) + $p_\pi$(Cl) set to the H-DAB $\pi^*$ occur at higher energy, the singlets at 3.83 and 3.89 eV, and the triplets at 3.34 and 3.72 eV. The singlet excitations can be assigned to the fourth band at ca. 4 eV.

A significant point to arise from our calculations is that the excited states accessible upon irradiation at ∼500 nm (2.5 eV) would not be by their electronic nature Mn−Cl dissociative, neither in the *fac*- nor in the *mer*-isomer. However, in both isomers photodissociation of the halide ligand could in principle still occur upon excitation in these MLCT states if the high lying LF states that are Mn−Cl $\sigma^*$ antibonding descend rapidly upon Mn−Cl bond bond lengthening and cross the MLCT states. Since the $^3(\sigma \rightarrow \sigma^*)$ excited state is dissociative and correlates asymptotically with the radical fragments in their ground states, this crossing would occur if the MLCT states are at higher energy than the ground-state energies of the fragments. The crossing may however be at too long Mn−Cl bond distance, so that a prohibitive barrier will exist on the first excited state (MLCT) surface. The MLCT states may actually be below the asymptotic energy, in which case the MLCT excitation simply does not provide enough energy to break the Mn−Cl bond. Significant reorganization of the complexes, just as in the case of the equatorial CO loss in the *fac*-Mn(Cl)(CO)$_3$(H-DAB),[10] may however lead to photoproducts with lower energy, thus enabling the photodissociation. These possibilities for the mechanism of Mn−Cl bond dissociation in *fac*- and in *mer*-isomers will be investigated in next section.

## 5. Photodissociation Mechanism of the Mn−Cl Bond in *fac*- and *mer*-Mn(Cl)(CO)$_3$(H-DAB)

**Molecular and Electronic Structure of the Five-Coordinated Primary Photoproducts.** To facilitate the discussion of the mechanisms of Cl loss in the *fac*- and *mer*-Mn(Cl)(CO)$_3$-(H-DAB) model complexes, we first consider the molecular

**Table 2.** Energies (eV) and Transition Dipole Moments (au) for Electronic Transitions in *fac*-(Cl)Mn(CO)$_3$(H-DAB)

| | | calculated singlets | | | | calculated triplets | |
|---|---|---|---|---|---|---|---|
| character | one-electron excitation | state | energy | transition dipole moments | experimental band maxima | state | energy |
| $d_{xz}$, $p_x$(Cl) →$\pi^*$(H-DAB) | 14a″→24a′ | $a^1A''$ | 1.60 | 0.001 | | $a^3A''$ | 1.50 |
| $d_{yz}$, $p_y$(Cl) →$\pi^*$(H-DAB) | 23a′→24a′ | $b^1A'$ | 1.71 | 0.052 | I 2.61 | $a^3A'$ | 1.53 |
| $d_{x^2-y^2}$→$\pi^*$(H-DAB) | 22a′→24a′ | $c^1A'$ | 2.18 | 0.005 | | $b^3A'$ | 2.14 |
| $p_x$(Cl), $d_{xz}$ →$\pi^*$(H-DAB) | 13a″→24a′ | $b^1A''$ | 3.02 | 0.008 | | $b^3A''$ | 2.81 |
| $p_y$(Cl), $d_{yz}$→$\pi^*$(H-DAB) | 21a′→24a′ | $d^1A'$ | 3.24 | 0.017 | II 3.45 | $c^3A'$ | 3.10 |
| $d_{xz}$, $p_x$(Cl) →$\sigma^*$ | 14a″→25a′ | $c^1A''$ | 3.41 | 0.012 | | $c^3A''$ | 2.91 |
| $d_{yz}$, $p_y$(Cl) →$\sigma^*$ | 23a′→25a′ | $e^1A'$ | 3.61 | 0.015 | | $e^3A'$ | 3.18 |
| $d_{xz}$, $p_x$(Cl) →$d_{xy}$ | 14a″→15a″ | $f^1A'$ | 3.68 | 0.059 | III 4.01 | $d^3A'$ | 3.08 |
| $d_{yz}$, $p_y$(Cl) →$d_{xy}$ | 23a′→15a″ | $d^1A''$ | 3.73 | 0.001 | | $d^3A''$ | 3.28 |

**Table 3.** Energies (eV) and Transition Dipole Moments (au) for Electronic Transitions in *mer*-Mn(Cl)$(CO)_3$(H-DAB)

| character | one-electron excitation | calculated singlets | | | experimental band maxima | calculated triplets | |
|---|---|---|---|---|---|---|---|
| | | state | energy | transition dipole moments | | state | energy |
| $d_{x^2-y^2} \rightarrow \pi^*$(H-DAB) | 37a → 38a | $b^1A$ | 1.55 | 0.002 | I 2.07 | $a^3A$ | 1.40 |
| $d_{xz(yz)} \rightarrow \pi^*$(H-DAB) | 36a → 38a | $c^1A$ | 1.89 | 0.047 | | $b^3A$ | 1.53 |
| $d_{yz(xz)} \rightarrow \pi^*$(H-DAB) | 35a → 38a | $d^1A$ | 2.55 | 0.079 | | $d^3A$ | 2.22 |
| $d_{x^2-y^2} \rightarrow \sigma^*$ | 37a → 39a | $e^1A$ | 2.72 | 0.005 | II 2.74 | $c^3A$ | 2.15 |
| $d_{xz}, p_z$ (Cl) $\rightarrow \sigma^*$ | 36a → 39a | $f^1A$ | 2.99 | 0.005 | | $e^3A$ | 2.57 |
| $d_{x^2-y^2} \rightarrow 2\pi^*$(CO) | 37a → 40a | $g^1A$ | 3.29 | 0.023 | | $f^3A$ | 2.91 |
| $d_{xz} \rightarrow 2\pi^*$(CO) | 36a → 40a | $h^1A$ | 3.51 | 0.060 | III 3.44 | $h^3A$ | 3.19 |
| $d_{xz,yz} \rightarrow 2\pi^*$(CO) | 36a → 41a | $i^1A$ | 3.62 | 0.015 | | $m^3A$ | 3.47 |
| $d_{x^2-y^2} \rightarrow 2\pi^*$(CO) | 37a → 41a | $l^1A$ | 3.65 | 0.031 | | $g^3A$ | 3.12 |
| $d_{x^2-y^2} \rightarrow 2\pi^*$(CO) | 37a → 42a | $m^1A$ | 3.82 | 0.005 | | $l^3A$ | 3.47 |
| $p_z$(Cl) $\rightarrow \pi^*$(H-DAB) | 34a → 38a | $n^1A$ | 3.83 | 0.061 | IV 4.0 | $i^3A$ | 3.34 |
| $p_{x,y}$(Cl) $\rightarrow \pi^*$(H-DAB) | 33a → 38a | $o^1A$ | 3.89 | 0.003 | | $n^3A$ | 3.72 |

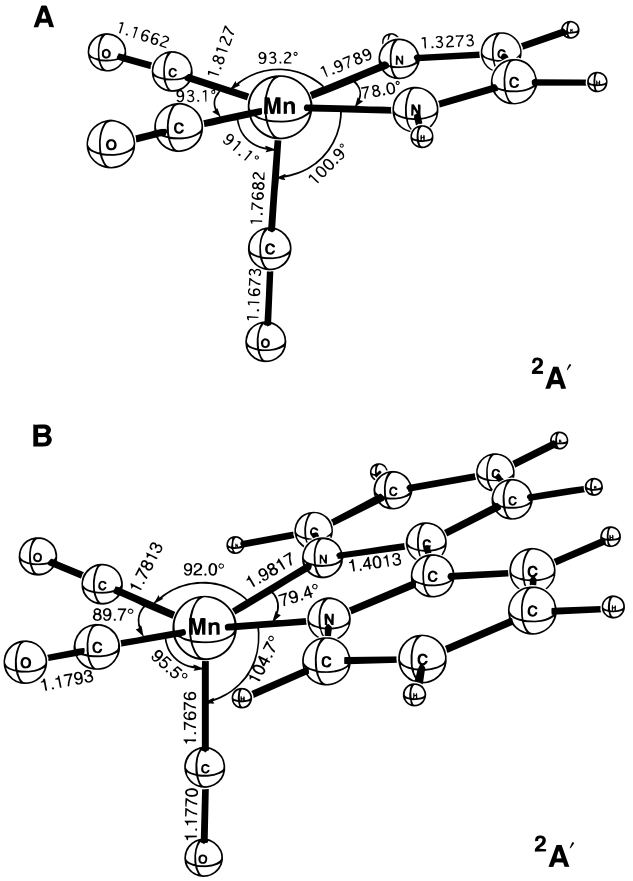


**Figure 3.** Optimized structures of [Mn$(CO)_3$(H-DAB)]• (A) and [Mn$(CO)_3$(bpy)]• (B) in $C_s$ symmetry.

structures of the five-coordinated primary products of the photodissociation.

Starting from the two basic structures **1a** and **1b** (see Chart 1) for [Mn$(CO)_3$(H-DAB)]• corresponding to the removal of the axial Cl• from the *fac*-Mn(Cl)$(CO)_3$(H-DAB) and of the equatorial Cl• from the *mer*-Mn(Cl)$(CO)_3$(H-DAB), respectively, a complete geometry optimization afforded in both cases the structure given in Figure 3A. This axial vacancy structure, which has $C_s$ symmetry and a $^2A'$ electronic ground state, has not rearranged much from the axial vacancy starting point, **1a**, but very much so from the equatorial vacancy structure **1b**. The energy lowering due to the geometrical relaxation of the five-coordinated fragments **1a** and **1b** amounts to 12 kJ/mol (0.13 eV) and 116 kJ/mol (1.2 eV), respectively. The large relaxation energy computed for the **1b** structure indicates that the shift of an axial CO to an equatorial open site is highly favored.

**Table 4.** Mn−Cl Bond Dissociation Energy, $D_e$(Mn−Cl) (kJ/mol), of *fac*-Mn(Cl)$(CO)_3$(H-DAB), *mer*-Mn(Cl)$(CO)_3$(H-DAB), and *mer*-Mn(Cl)$(CO)_3$(bpy) for Frozen-Geometry Fragments and Geometry-Optimized

| geometry of the fragments | *fac*-Mn(Cl) $(CO)_3$(H-DAB) | *mer*-Mn(Cl) $(CO)_3$(H-DAB) | *mer*-Mn(Cl) $(CO)_3$(bpy) |
|---|---|---|---|
| frozen[a] | 280 | 360 | 349 |
| optimized | 268 | 244 | 269 |

[a] Geometries of the five-coordinate fragments are fixed to those in the corresponding complexes.

The high instability of the [Mn$(CO)_3$(H-DAB)]• fragment in the equatorial vacancy structure **1b** appears to be typical of a Mn ($d^6$) α-diimine five-coordinated fragment. If we take bipyridine as the α-diimine ligand, a complete geometry optimization of [Mn$(CO)_3$(bpy)]• starting with the **1b** type structure corresponding to the removal of the equatorial Cl• from the *mer*-Mn(Cl)$(CO)_3$(bpy) yields the structure given in Figure 3B in which again the axial CO has moved to the equatorial site. This structure, with $C_s$ symmetry and a $^2A'$ electronic state, is 80 kJ/mol (0.83 eV) more stable than the frozen **1b**, which is somewhat less than the 116 kJ/mol found for the complex with the H-DAB ligand. The high relaxation energy does not depend on the axial ligand being CO. If an equatorial vacancy is created by removal of an equatorial CO ligand from the *fac*-Mn(Cl)$(CO)_3$(H-DAB), the unrelaxed Mn(Cl)$(CO)_2$(H-DAB) structure (**1b**-type, with a Cl substituted for one of the axial COs) is similarly highly unstable and we have previously found[10] that it rearranges to a structure analogous to those of Figure 3, i.e., a distorted square pyramid structure characterized by pronounced bending of the axial halide toward the vacant equatorial site. This structure is 59 kJ/mol (0.61 eV) more stable than the frozen structure.

These findings for the energetics of axial and equatorial Mn−Cl bond homolysis are summarized in Table 4. It exhibits both the small (12 kJ/mol) relaxation of the structure with an axial vacancy in the case of *fac*-Mn(Cl)$(CO)_3$(H-DAB), and the much larger relaxation energies of the equatorial vacancy structures in case of *mer*-Mn(Cl)$(CO)_3$(α-diimine), 116 and 80 kJ/mol for α-diimine = H-DAB and bpy, respectively. Although the axial Cl has a considerably lower bond energy than the equatorial Cl—280 versus 360 kJ/mol—with respect to the frozen structures, the much larger relaxation in the latter case causes the Cl coordination energy to be ultimately rather similar in the *fac*- and *mer*-isomers. In fact, the relaxation even overcompensates in the case of H-DAB, making the bond energy for equatorial Cl (244 kJ/mol) some 24 kJ/mol lower than for the axial Cl (268 kJ/mol). Direct comparison of these data with experiment is not possible because the energetics of the *fac*- and *mer*-Mn-

**Table 5.** One-Electron Energy and Percentage Composition (Based on Mulliken Population Analysis per MO) from Spin-Restricted Calculations of the Lowest Unoccupied and Highest Occupied Orbitals of the $[Mn(CO)_3(H-DAB)]^\bullet$ Fragment in Its Relaxed Doublet Ground State Structure (Figure 3A)

| MO | $\epsilon$ (eV) | occ.[a] | Mn | $CO_{eq}$ | $CO_{ax}$ | H-DAB |
|---|---|---|---|---|---|---|
| 22a′ | −2.74 | 0 | 20($d_{z^2}$); 17($d_{yz}$); 8($4p_z$) | 13($2\pi^*_\perp$) | 5($5\sigma$); 3($2\pi^*$) | 34($\pi^*$) |
| 21a′ | −4.63 | 1 | 18($d_{z^2}$); 11($4p_z$) | 18($2\pi^*_\perp$) | − | 53($\pi^*$) |
| 13a″ | −5.54 | 2 | 64($d_{xz}$) | 13($2\pi^*_\perp$) | 15($2\pi^*$) | 8($\pi$) |
| 20a′ | −5.66 | 2 | 59($d_{x^2-y^2}$); 11($d_{yz}$) | 24($2\pi^*_{||}$) | − | 6($\pi^*$) |
| 19a′ | −5.87 | 2 | 48($d_{yz}$); 11($d_{x^2-y^2}$); 5($d_{z^2}$) | 9($2\pi^*_\perp$);5($2\pi^*_{||}$) | 15($2\pi^*$) | 7($\pi^*$) |

[a] Orbital occupancy.

**Table 6.** One-Electron Energy and Percentage Composition (Based on Mulliken Population Analysis per MO) from Spin-Restricted Calculations of the Lowest Unoccupied and Highest Occupied Orbitals of the $[Mn(CO)_3(H-DAB)]^\bullet$ Fragment in Its Doublet Unrelaxed **1b** Structure

| MO | $\epsilon$ (eV) | occ.[a] | Mn | $CO_{eq}$ | $CO_{ax}$ | H-DAB |
|---|---|---|---|---|---|---|
| 35a | −3.60 | 0 | 18($d_{yz}$); 2($d_{xz}$) | − | 4($5\sigma$);6($2\pi^*$) | 70 ($\pi^*$) |
| 34a | −3.72 | 1 | 24($d_{xy}$); 18($d_{z^2}$); 16($4p_{x,y}$);4($d_{x^2-y^2}$) | 3($2\pi^*_{||}$) | 3($5\sigma$);28($2\pi^*$) | 4 (N-lp) |
| 33a | −4.88 | 2 | 74($d_{x^2-y^2}$); 3($d_{z^2}$) | 13($2\pi^*_{||}$); 6($2\pi^*_\perp$) | 4($2\pi^*$) | − |
| 32a | −5.25 | 2 | 50($d_{xz}$); 9($d_{yz}$) | 6($2\pi^*_\perp$) | 17($2\pi^*$) | 11($\pi^*$); 7($\pi$) |
| 31a | −5.80 | 2 | 43($d_{yz}$); 14($d_{xz}$) | 6($2\pi^*_\perp$) | 15($2\pi^*$) | 16($\pi^*$); 5 ($\pi$) |

[a] Orbital occupancy.

(Cl)$(CO)_3$(α-diimine) complexes has never been investigated. Nevertheless we note that the computed $D_e(Mn-Cl_{ax})$ value of 268 kJ/mol fits in with the $\Delta H$ (Mn−Cl) value of 268 kJ/mol measured for the parent Mn(Cl)$(CO)_5$ complex.

The Mn−Cl dissociation energies computed for the *fac*- and *mer*-isomers point to the higher thermodynamic stability of the Mn−Cl bonds compared to Mn−CO bonds that we have already observed in Mn(Cl)$(CO)_5$.[9] We have found[10] that in the *fac*-Mn(Cl)$(CO)_3$(H-DAB) the dissociation energy of the axial CO amounts to 174 kJ/mol (1.80 eV), whereas the first equatorial CO dissociation energy is 122 kJ/mol (1.26 eV). For the *mer*-isomer the dissociation energy computed for the axial and the equatorial COs amounts to 96 kJ/mol (1.00 eV) and 94 kJ (0.97 eV), respectively. These values include the relaxation of the resulting metal fragment.

There is experimental evidence[4a] for the axial vacancy structure **1a** of the structure of the five-coordinated $[Mn(CO)_3$(α-diimine)$]^\bullet$ intermediate resulting from the Mn−Cl bond homolysis photoreaction observed in the *mer*-Mn(Cl)$(CO)_3$(α-diimine) complexes (*fac*-Mn(Cl)$(CO)_3$(α-diimine) complexes do not show Mn−Cl bond homolysis). Also earlier ESR measurements[32] are relevant. The *g* factors found for these radicals are rather close to the free electron value ($g = 2.003$) and different from the *g* factors found for Mn-centered radicals,[33] which usually have higher *g* values. This suggests that the unpaired electron resides at the α-diimine ligand and the radicals have been considered to be best represented as 16e complexes in which $Mn^+(d^6)$ is surrounded by three carbonyl groups and a bidentate α-diimine ligand, which is a radical anion being negatively charged by the 17th (unpaired) electron residing in its $\pi^*$ orbital. The ESR studies[32] of the adducts with nucleophilic ligands such as phosphines, pyridine, and *t*-Bu-NO have indicated that the nucleophile coordinates to the metal in an axial position. The pseudo square pyramidal structure with two COs in the equatorial metal−α-diimine plane and an axial vacancy that has been proposed for these radicals on the basis of the experimental results is in agreement with the present theoretical results. Also the formation of $Mn_2(CO)_6$(α-diimine)$_2$ dimers in the last reaction step of Scheme 1 supports the axial vacancy structure. The dimerization process is indeed much easier when the $[Mn(CO)_3$(α-diimine)$]^\bullet$ radicals are in a configuration with an axial rather than an equatorial vacancy, since no structural rearrangements are involved.

**Scheme 4**

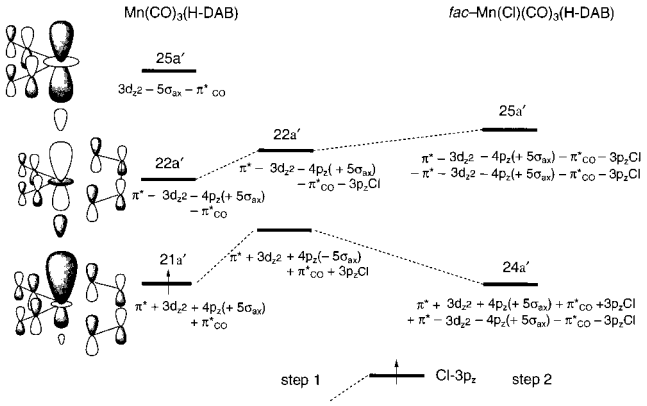


It is at first sight surprising that the unpaired electron on the metal fragment is pictured to have DAB-$\pi^*$ character rather than metallic (hybrid $d_{z^2}/4p_z$) character. The bond with Cl (or a one-electron aliphatic R ligand like methyl or ethyl) to form *fac*-Mn(Cl or R)$(CO)_3$(α-diimine), is certainly made with the metal and not with the α-diimine. In Table 1a the 20a′ $\sigma$-bonding orbital has very little DAB-$\pi^*$ character indeed. Since in the next section we will consider the photochemical breaking of the metal−Cl $\sigma$ bond in *fac*-Mn(Cl)$(CO)_3$(α-diimine), we briefly address here this particular electronic structure aspect.

In Table 5 the energy and composition of the frontier orbitals of the Mn$(CO)_3$(DAB) moiety are presented. It is interesting to observe that there is indeed, in agreement with the inferences from the ESR data, a high percentage (53%) of DAB-$\pi^*$ character in the unpaired spin−orbital 21a′, although it is by no means a pure α-diimine $\pi^*$ orbital. There is also considerable $\pi^*$ character in the next higher orbital, 22a′. As a matter of fact, the composition of these orbitals can be directly compared to the analogous frontier orbitals of Mn$(CO)_5$ which have been analyzed in ref 11a. We picture these orbitals in Scheme 4 and note that the Mn$(CO)_3$(DAB) system only differs from Mn$(CO)_5$ in that there are now, in addition to the metal-centered $d_{z^2}$ and $4p_z$ orbitals, two ligand centered orbitals of the same symmetry involved, a $CO_{eq}$ $\pi^*$ combination of a′

(32) Andréa, R. R.; de Lange, W. G.; van der Graaf, T.; Rijkhoff, M.; Stufkens, D. J.; Oskam, A. *Organometallics* **1988**, *7*, 1100.
(33) Gross, R.; Klaim, W. *Angew. Chem., Int. Ed. Engl.* **1980**, *24*, 856.

symmetry and the DAB-$\pi^*$ of the same symmetry (in $Mn(CO)_5$ there is only a single $a_1(CO_{eq}$-$\pi^*)$ combination). The DAB-$\pi^*$, being lower in energy, dominates over the $CO_{eq}$ $\pi^*$ in the ligand centered part of the 21a′ and 22a′ MOs, but for the rest the situation is perfectly analogous to the one in $Mn(CO)_5$, for which a detailed explanation was provided in ref 11a: the SOMO, analogous to $10a_1$ of $Mn(CO)_5$, has much ligand character ($\pi^*$ of α-diimine and $CO_{eq}$), and apart from the expected $d_{z^2}$ character also considerable $4p_z$ character (the $4p_z$ plays a crucial role in the orbital interactions giving rise to these frontier orbitals). The next higher orbital, 22a′, analogous to the $11a_1$ of $Mn(CO)_5$, has the features discussed earlier,[11a] in particular the opposite phases of $\pi^*$ and $d_{z^2}$ as compared to 21a′, cf. Scheme 4. We note that the free-electron *g* value obtained experimentally fits in with considerable gaps between the unpaired electron orbital and the next higher and lower orbitals, and with the relatively large ligand character (much $\pi^*$(DAB) but also $CO_{eq}$-$\pi^*$) which minimizes effects of spin−orbit coupling.

If we now compare the orbital compositions for $Mn(CO)_3$(DAB) in Table 5 and Scheme 4 to the orbital composition of *fac*-$Mn(Cl)(CO)_3$(α-diimine) in Table 1a, the concentration of DAB-$\pi^*$ character in the 24a′ LUMO of *fac*-$Mn(Cl)(CO)_3$(α-diimine) is quite striking. It agrees with the intuitive assumption that the electron pair bond between Cl and the metal fragment radical does not involve an α-diimine-Cl bond but a metal-Cl bond, which is in fact constituted by the occupied 20a′/unoccupied 25a′ $\sigma/\sigma^*$ pair. Scheme 4 depicts the somewhat miraculous disappearance of DAB-$\pi^*$ character from this bond: in a first orbital interaction step the Cl-$3p_z$ AO pushes the 21a′ and 22a′ (less) up. The perturbed orbitals next mix in the second step where the phases are such that in the 24a′ that is formed the DAB-$\pi^*$ character is enhanced and all other contributions diminished, whereas in the 25a′ the reverse happens. The 24a′ thus emerges as the mostly DAB-$\pi^*$ orbital and the 25a′ as the Cl-$3p_z$-Mn-$3d_{z^2}(4p_z)$ $\sigma^*$ orbital.

We will now first discuss the Mn−Cl bond breaking in the *fac*-isomer, which will, according to our results thus far, involve little geometrical relaxation of the resulting axial vacancy structure, but considerable electronic structure reorganization. Equatorial Cl photodissociation, however, to be discussed next, either has to involve a strong rearrangement of the complex during Cl departure, or the equatorial vacancy fragment **1b** is first formed and subsequently interconverts into the much more stable axial vacancy structure. The possible consequences of this difference between *fac*- and *mer*-isomers for the mechanism of Cl photodissociation, and indeed the absence versus presence of photolysis in the two cases, will be explored employing explicit PEC calculations.

**Explanation for the Absence of Photolysis of the Axial Cl Ligand in *fac*-Mn(Cl)(CO)$_3$(H-DAB) using Potential Energy Curves.** The potential energy curves along the Mn−Cl coordinate for the ground state and the $^{1,3}A''$ and $^{1,3}A'$ excited states that belong (at the equilibrium distance) to the lowest energy band centered at 526 nm (2.36 eV) are displayed in Figure 4. According to elementary spin and symmetry correlation rules, the ground state, $a^1A'$, as well as the $a^{1,3}A''$, $b^1A'$, $a^3A'$, and $b^3A'$ excited states asymptotically correspond to the $^2A'$ ground state of $[Mn(CO)_3(H\text{-}DAB)]^\bullet$ and the $^2P$ ground state of $Cl^\bullet$. The latter corresponds in $C_s$ symmetry to two $^2A'$ states (electron hole in either Cl-$3p_z$ or in-plane $3p_\pi$) and one $^2A''$ (electron hole in perpendicular $3p_\pi$). The $c^1A'$ which could also be accessed by irradiation into the first band, correlates with the first $a^2A''$ excited state of the five-coordinated fragment and has a bound PEC. Of course only the singlet states can be accessed by allowed transitions, and in fact only the $b^1A'$ has a significant transition dipole moment, cf. Table 2.

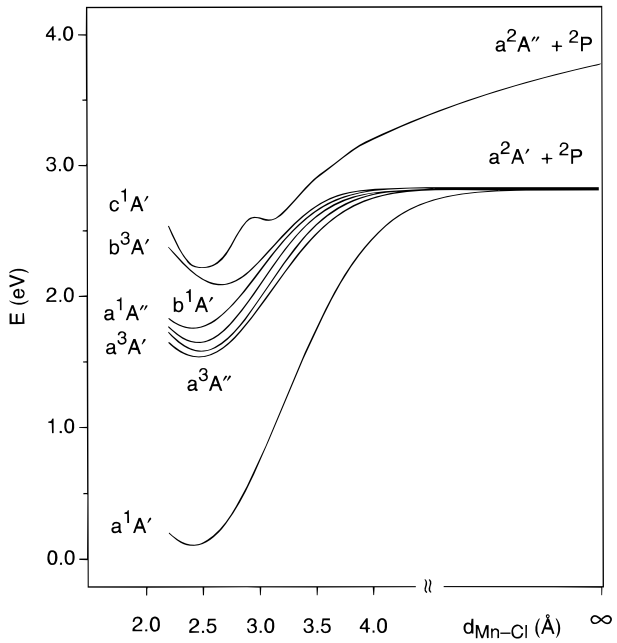


**Figure 4.** Potential energy curves for the dissociation of the Mn−Cl bond in *fac*-$Mn(Cl)(CO)_3$(H-DAB).

The first four states, $a^3A''$, $a^3A'$, $a^1A''$, and $b^1A'$, correspond to $d_\pi/p_\pi(14a'', 23a') \rightarrow \pi^*(24a')$ excitations. Along the Mn−Cl coordinate the electronic character will change, since the 25a′-($\sigma^*$) will come down in energy and will effectively mix with the $\pi^*$ (24a′) to form the SOMO of $Mn(CO)_3$(H-DAB) (containing the "excited" electron). This was extensively discussed in the previous section. In the occupied orbital spectrum, three orbitals (two $3p_\pi$, one $3p_\sigma$) will along the Mn−Cl dissociation coordinate develop into 100% Cl 3p orbitals. In fact, the occupied orbital spectrum of the $[Mn(CO)_3$(H-DAB)]$^\bullet$ fragment in Table 5 derives directly from that of *fac*-$Mn(Cl)(CO)_3$(H-DAB) in Table 1a by removing the low-lying occupied Cl orbitals from the one-electron level spectrum. Although the electron hole initially is in the 14a″ or 23a′, it cannot remain in these orbitals along the Mn−Cl dissociation coordinate since they develop into the 13a″ and 20a′ $t_{2g}$-$d_\pi$ orbitals of the $[Mn(CO)_3$(H-DAB)]$^\bullet$ fragment (see Table 5). This would imply that a $[Mn(CO)_3(H\text{-}DAB)]^+$ ion would result, and a $Cl^-$ ion as well since the Cl 3p orbitals remain fully occupied. The electron hole will ultimately have to reside in one of the Cl $3p_\pi$ orbitals, which develop from the bonding 13a″, 21a′ of *fac*-$Mn(Cl)(CO)_3$(H-DAB) (Table 1a). So along the $a^3A''$, $a^3A'$, $a^1A''$, and $b^1A'$ PECs an avoided crossing with initially higher lying states with 13a″ → $\pi^*$ (24a′) character, and 22a′ → 24a′, and subsequently 21a′ → 24a′ character, changes the electronic character to the desired one with a hole in a Cl $3p_\pi$ (13a″ and 21a′ become Cl $3p_\pi$ orbitals). The next higher states, $b^3A'$ and $c^1A'$, correspond at $R_e$ to $d_{x^2-y^2} \rightarrow \pi^*$ (22a′ → 24a′) excitation. The $b^3A'$ exhibits an avoided crossing with the originally high lying triplet state arising from the $\sigma \rightarrow \sigma^*$(20a′ → 25a′) excitation. According to the usual behavior of an electron pair bond, the potential energy curve of this state will be purely dissociative and it will correlate asymptotically with the products in their ground states. (The singlet $^1(\sigma \rightarrow \sigma^*)$ correlates with ions and does not interfere with the low-lying states under consideration.) The electronic nature of $b^3A'$ changes accordingly from $d_{x^2-y^2} \rightarrow \pi^*$ at $R_e$ to $\sigma \rightarrow \sigma^*$ asymptotically, where

the hole is in the Cl-$p_z$ and the electron in the $Mn(CO)_3$(H-DAB) SOMO. Translated back to an orbital picture, the 20a′, which is in *fac*-Mn(Cl)$(CO)_3$(H-DAB) the bonding orbital between Cl-$p_z$ and the metal fragment, will destabilize during the Mn−Cl dissociation, and eventually "pick up" the hole from the $d_{x^2-y^2}$, which is higher (22a′) at $R_e$. The singlet $c^1A'$ behaves in a different way and correlates at the dissociation limit with the first $a^2A''$ excited state of the five-coordinated fragment [Mn$(CO)_3$(H-DAB)]• which lies 1.09 eV above its ground state.

The most important feature of Figure 4 is that all of the states corresponding to the first absorption band have energies that are at $R_e$ well below the asymptotic energy of the photoproducts, the five-coordinated fragment and the Cl atom. Therefore Mn−Cl bond homolysis cannot occur upon irradiation into the first band, which agrees with the absence of this homolysis in the photochemical experiments. The absence of Mn−Cl bond homolysis can be attributed both to the high thermodynamic stability of this bond and the low energy of the lowest MLCT states of the *fac*-Mn(Cl)$(CO)_3$(H-DAB).

**Discussion of the photolysis of the Equatorial Cl Ligand in *mer*-Mn(Cl)$(CO)_3$(α-diimine) using calculated Potential Energy Curves for α-Diimine = H-DAB.** Our calculations have shown that the primary photoproduct following Cl loss in the *mer*-Mn(Cl)$(CO)_3$(α-diimine) complexes adopts the Figure 3A (or 3B) structure. This implies that either the equatorial Cl photodissociation occurs with simultaneous strong rearrangement of the complex leading directly to the Figure 3 fragment, or the unrelaxed five-coordinated **1b** fragment interconverts into the Figure 3 fragment immediately *after* its formation. However, based on energetics arguments, we may exclude that the initial product following Cl loss in the *mer*-Mn(Cl)$(CO)_3$(α-diimine) complexes could be the five-coordinated fragment in the unrelaxed **1b** structure. In fact, the 2.5 eV excitation energy experimentally used is far below the asymptotic ground-state energy of the radicals Cl• and [Mn$(CO)_3$(H-DAB)]• in the frozen **1b** geometry, which according to Table 4 amounts to 3.73 eV (360 kJ/mol). Therefore, even though the lowest excited states do correlate with the ground states of the radicals, the Mn−Cl bond homolysis cannot occur in the case of retention of the atomic configuration. This would also be true for the *mer*-Mn(Cl)$(CO)_3$(bpy), since the dissociation of this complex into the ground states of the radicals, [Mn$(CO)_3$(bpy)]• in the frozen **1b** geometry and Cl•, would require, according to the data reported in Table 4, 3.62 eV (349 kJ/mol).

These arguments suggest that the initial product following Cl loss in the *mer*-Mn(Cl)$(CO)_3$(H-DAB) should be the Figure 3A [Mn$(CO)_3$(H-DAB)]• fragment and the bending of one axial CO toward the equatorial position should be concomitant with the Mn−Cl bond elongation.

In view of the fact that the most relevant geometrical change observed in this fragment is the displacement of one axial CO toward the vacant equatorial site, only the angle $\theta$ that the axis of one of the Mn−$CO_{ax}$ bonds makes with the vertical $z$ axis has been optimized on the ground-state curve along the reaction pathway corresponding to the Mn−Cl bond elongation. Our calculations show that $\theta$ increases from 11 initially to 31°, 43°, and 65° upon elongation of the Mn−Cl bond from $R_e$ to 4.0, 4.5, and 5.0 Å, respectively. This structural rearrangement is responsible for the potential barrier on the ground-state PEC, with a maximum (ca. 0.3 eV above the asymptotic energy) around 4.0 Å, see Figure 5. The excited-state PECs have been calculated using at each Mn−Cl distance the ground-state geometry.

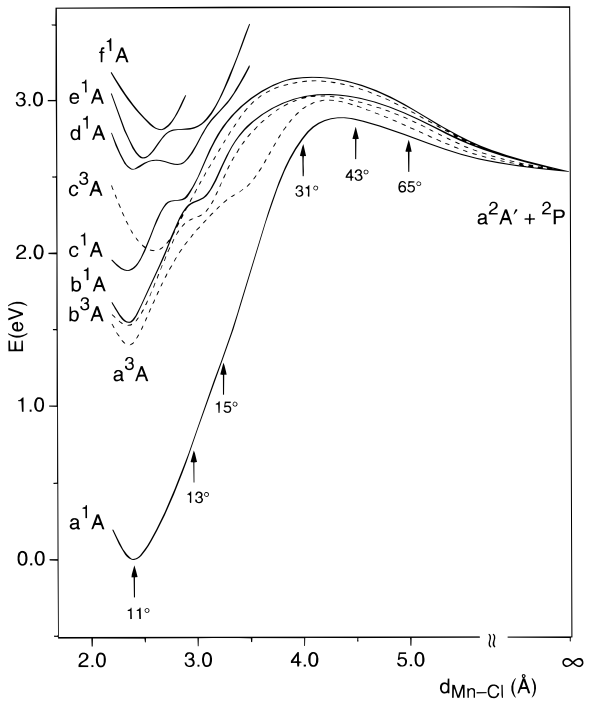


**Figure 5.** Potential energy curves for the dissociation of the Mn−Cl bond in *mer*-Mn(Cl)$(CO)_3$(H-DAB).

There are six states that asymptotically correlate with the $^2A'$ + $^2P$ ground states of [Mn$(CO)_3$(H-DAB)]• and Cl• radicals: besides the ground state, $a^1A$, also the excited states corresponding at $R_e$ to the excitations out of the antibonding $d_\pi/p_\pi$ 36a, 37a orbitals (see Table 1b) to the $\pi^*$(H-DAB) 38a LUMO, i.e., the triplet and singlet $d_{x^2-y^2} \rightarrow \pi^*$, ($a^3A$, $b^1A$), the triplet and singlet $d_{xz(yz)} \rightarrow \pi^*$, ($b^3A$, $c^1A$), and the triplet 37a ($d_{x^2-y^2}$) → 39a ($\sigma^*$) ($c^3A$). These PECs are all displayed in Figure 5. The next six excited states are the singlets $d^1A$, $e^1A$, and $f^1A$ corresponding at $R_e$ to the $d_{yz(xz)} \rightarrow \pi^*$(H-DAB) (35a → 38a), to the $d_{x^2-y^2} \rightarrow \sigma^*$ (37a → 39a) and to the $d_{xz(yz)} \rightarrow \sigma^*$ (36a → 39a) excitations respectively, and the triplets $d^3A$, $e^3A$, and $f^3A$ corresponding at $R_e$ to the $d_{yz(xz)} \rightarrow \pi^*$(H-DAB) (35a → 38a), the $d_{xz(yz)} \rightarrow \sigma^*$ (36a → 39a) and the $d_{x^2-y^2} \rightarrow 2p^*$(CO) (37a → 40a) excitations, respectively. All these states will correlate asymptotically with the first $a^2A''$ excited state of the five-coordinated fragment [Mn$(CO)_3$(H-DAB)]• that lies 1.09 eV above its ground state and the $^2P$ ground state of Cl•. The potential energy curves of these states have been computed only for Mn−Cl bond lengths ≤3.5 Å and the singlets $d^1A$, $e^1A$, and $f^1A$ are shown in Figure 5 (the triplets are not shown for sake of clarity). It is interesting to note that, in the range of Mn−Cl bond lengths where the complex substantially retains its equilibrium geometry (2.2−3.3 Å), the shape of several PECs is affected by avoided crossings.

As inferred from Figure 5, none of the excited state PECs correlating asymptotically with the $^2A'$ + $^2P$ ground states of [Mn$(CO)_3$(H-DAB)]• and Cl• radicals has a dissociative character. The asymptotic energy is much higher than the energy they have at the equilibrium geometry, and, in addition, a quite high potential barrier prevents Cl loss to occur along these states. Mn−Cl photodissociation cannot occur either along the next six excited states because the asymptotic energy (not shown in the figure; corresponding to an excited state of [Mn$(CO)_3$(H-DAB)]•) is much higher than the energy at $R_e$.

Although Cl loss cannot occur directly along the excited-state PECs of the *mer*-Mn(Cl)$(CO)_3$(H-DAB) accessible upon irradiation with 2.5 eV radiation, our calculations suggest that

Mn−Cl bond homolysis might occur through an alternative mechanism, which is suggested by the topology of the ground-state PEC, with its characteristic maximum.

According to the well-known resonance phenomenon of continuum states above a potential well,[34] such states will at certain energies have a resonance-enhanced amplitude in the potential well region (around $R_e$) reminiscent of the vibrational states in the discrete part of the spectrum of vibrational states. Irradiation at ~2.5 eV (which for the *mer*-isomer is into the *second* band) will strongly populate the $d^1A$ state, with a high transition dipole moment (see Table 3). Radiationless decay from this $d^1A$ excited state to a continuum state belonging to the electronic ground state PEC, at approximately the same energy as the $d^1A$ state, may lead to dissociation. The continuum state will have an enhanced amplitude above the potential well provided by the ground state PEC, i.e. around $R_e$. This is also the region where the lowest vibrational states in the $d^1A$ PEC (which has a broad minimum) have high amplitude. Dissociation can occur directly if the transition takes place from the $d^1A$ state (maybe vibrationally excited) to a continuum state above the maximum of the barrier. If the transition is to a continuum state just below the maximum of the barrier, dissociation can still occur by thermal excitation (rather than tunneling). This process would of course occur on a much longer time scale than the fast ejection of a ligand along a dissociative PEC, making time available for the presumably slow motion of the axial CO to the equatorial position.

When the α-diimine is H-DAB, the dissociation mechanism sketched here actually has to compete with decay from the higher excited states to the first excited state. When an aromatic α-diimine ligand is used like bipyridine, the first excited states are lying at considerably higher energy, comparable to the states in the second band for α-diimine = H-DAB. These states, in the first band of $Mn(Cl)(CO)_3$(bpy), may then play the role that in our case, with the H-DAB ligand, could only be played by the excited states of the second band. The only requirement is that the photoactive excited state is lying above the asymptotic energy, i.e., the excitation energy should be sufficient to break the bond, and the photoactive excited states should be above or sufficiently close to the maximum on the ground state potential energy curve. The nature of the excited states does not seem to be relevant. Whether they are the lowest excited states, i.e., occur in the first absorption band, or are states in a second band, will be relevant to the extent that in the second case the alternative mechanism of decay to the lowest excited singlet state may be operative. Experimentally[4a] homolytic dissociation into $Cl^•$ and $[Mn(CO)_3(\alpha\text{-diimine})]^•$ radicals does occur, upon irradiation at 488 nm, if the first excited states are relatively highlying, i.e., for α-diimine = bipy and $^i$Pr-PyCa. There is no experimental evidence[4b] for the homolytic splitting for α-diimine = $^i$Pr-DAB, presumably since rapid conversion to the lowest excited state takes place, which is so low-lying that the barrier for homolytic splitting is prohibitive.

A second relevant point is of course, to what extent heterolytic CO loss will compete with the generation of $Cl^•$ radicals. This subject has not been pursued here, and would eventually require detailed dynamics calculations, of higher dimensionality, on very accurate potential energy surfaces, to establish relative yields.

## 6. Conclusions

We have been able to explain the observed photochemical homolytic Mn−Cl bond breaking in *mer*-$Mn(Cl)(CO)_3$(α-diimine) systems, as well its absence in the *fac*-isomers. The dissociation mechanism invoked here, involving ligand rearrangement during the Cl departure, in a continuum state above the ground-state potential energy surface, is analogous to the one we have proposed for the Mn−$CO_{eq}$ bond breaking in the *fac*-isomer.[10] The dissociation of an equatorial CO in the *fac*-isomer also leads to a ground state PEC with a clear maximum reflecting the reorganization of the metal fragment which consists of migration of the axial Cl to the vacated equatorial position. In that case the proposed mechanism explains the possibility of equatorial CO dissociation, and is in agreement with the experimentally observed photochemical *fac* to *mer* isomerization, because back-reaction with a CO would lead to the *mer*-isomer, with Cl in the equatorial plane. In the present case this mechanism is able to explain the observed homolytic Mn−Cl bond splitting in the *mer*-isomer which we set out to elucidate. We therefore conclude that the mechanism identified here is probably not an esoteric one, but has generally to be taken into account as a possible route to metal−ligand photodissociation in the rationalization of experimentally observed TM photochemistry.

We have noted that dissociation according to this mechanism will probably occur on a much longer time scale than the rapid ejection of a ligand along a purely dissociative PES.[35] It would be interesting to see experimental investigations of this point.

IC980757F

(34) Messiah, H. *Quantum Mechanics*: North-Holland: Amsterdam, 1963: Vol. 1, Chapter III.6.

(35) (a) Joly, A. G.; Nelson, K. A. Becke, A. *Chem. Phys.* **1991**, *152*, 69. (b) Lian, T.; Bromberg, S. E.; Asplund, M. C.; Yang, H.; Harris, C. B. *J. Phys. Chem.* **1996**, *100*, 11994.